A&A 379, 1123–1137 (2001)
DOI: 10.1051/0004-6361:20011352

Astronomy & Astrophysics

SPH simulations of clumps formation by dissipative collisions of molecular clouds

II. Magnetic case

E. P. Marinho[1], C. M. Andreazza[1], and J. R. D. Lépine[2]

[1] Instituto de Geociências e Ciências Exatas, Departamento de Estatística, Matemática Aplicada e Computação, UNESP, Rua 10, 2527, 13500-230 Rio Claro SP, Brazil
[2] Instituto Astronômico e Geofísico, Departamento de Astronomia, USP, Av. Miguel Stefano, 4200, 04301-904 São Paulo SP, Brazil

Received 15 Mars 2001 / Accepted 24 September 2001

Abstract. We performed computer simulations of interstellar cloud-cloud collisions using the three-dimensional smoothed particle magnetohydrodynamics method. In order to study the role of the magnetic field on the process of collision-triggered fragmentation, we focused our attention on head-on supersonic collisions between two identical spherical molecular-clouds. Two extreme configurations of the magnetic field were adopted: parallel and perpendicular to the initial clouds motion. The initial magnetic field strength was approximately 12.0 μG. In the parallel case, much more of the collision debris were retained in the shocking region than in the non-magnetic case where gas escaped freely throughout the symmetry plane. Differently from the non-magnetic case, eddy-like vortices were formed. The regions of highest vorticity and the the regions of highest density are offset. We found clumps formation only in the parallel case, however, they were larger, hotter and less dense than in the analogous non-magnetic case. In the perpendicular case, the compressed field works as a magnetic wall, preventing a stronger compression of the colliding clouds. This last effect inhibits direct contact of the two clouds. In both cases, we found that the field lines show a chaotic aspect in large scales. Also, the field magnitude is considerably amplified in the shock layer. However, the field distribution is almost coherent in the higher density regions.

Key words. methods: numerical – MHD – ISM: clouds – ISM: molecules – ISM: magnetic field

1. Introduction

The star-formation activity in NGC 1333 (Loren 1976), W49N (Miyawaki et al. 1986; Serabyn et al. 1993; Buckley & Ward-Thompson 1996), SgrB2 (Hasegawa et al. 1994), and in the cometary cloud G110-3 (Odenwald et al. 1992), among other star-forming regions, has been interpreted in terms of star formation triggered by collision between interstellar clouds. On the other hand, there are observational evidences that cloud-cloud collision may occur without star-formation, as in Heiles 2 (Little et al. 1978), Draco nebula (Rohlfs et al. 1989), LVC 127 (Meyerdierks 1992), and in IRAS 2306+1451 (Vallée 1995), for instance. These observational results show that the study of interstellar cloud collisions is of great importance not only to understand in what conditions they can trigger star formation, but also to understand how does cloud-cloud collision affect the structure and evolution of the interstellar medium.

Send offprint requests to: E. P. Marinho,
e-mail: emarinho@rc.unesp.br

Several analytical and numerical hydrodynamics studies of collisions between interstellar clouds have been made to investigate different aspects of this process (Stone 1970a, 1970b; Hausman 1981; Gilden 1984; Lattanzio et al. 1985; Keto & Lattanzio 1989; Habe & Ohta 1992; Pongracic et al. 1992; Kimura & Tosa 1996; Ricotti et al. 1997; Miniati et al. 1997; Klein & Woods 1998; Marinho & Lépine 2000). The final outcome of an individual collision event, like disruption, coalescence, fragmentation, and star formation, depends on many factors, like the density, shape and size of the clouds, their relative velocity and impact parameter, and on the details of the gas cooling mechanism, which in turn depends on metallicity etc.

Very few works have been addressed to magnetized cloud-cloud collisions. In their previous attempts to model the interactions between diffuse magnetized clouds, Clifford & Elmegreen (1983) found that the magnetic field enhances the exchange of momentum between clouds, so that the effective cross section is larger than the cloud's

geometric cross section. Elmegreen (1988) studied collision fronts of magnetized clouds, and showed an enhancement on both the density and the probability of gravitational collapse in the parts of molecular clouds that are compressed parallel to the mean field. In contrast, he found that the collisional dissipation and the compression are small for the parts of the clouds that are compressed perpendicular to the field.

More recently, using a two-dimensional magnetohydrodynamical model, Miniati et al. (Miniati et al. 1999) simulated a head-on collision of two identical diffuse clouds, with a weak magnetic field (1.2 μG). They found that the cloud-cloud collision with the initial field lines oriented parallel to the clouds velocity leads to almost complete coalescence of the clouds, and that the clouds moving perpendicular to the initial magnetic field forms a magnetic shield in front of both clouds. This last effect inhibits direct contact of the two clouds. Finally, Santillán et al. (1999) simulated collisions of high velocity clouds with a magnetized galactic disk, at different incidence angles and velocities, and showed that the interactions prevent the mass exchange between the halo and the disk. The collision can transform a high-velocity inflow into an outflow with vertical gas structures. These results indicate a strong influence of the magnetic field when it is perpendicular to cloud relative velocity.

It is increasingly clear that the magnetic field is a crucial component of the physics governing the evolution of interstellar clouds and star formation. Magnetic fields have been detected throughout our Galaxy. Observations suggest that the overall direction of polarization is roughly parallel to the galactic disk (e.g. Zeldovich et al. 1983). Moreover, the field is found to consist of an ordered component, which is coherent over a few kiloparsecs, and a disordered or turbulent component, which varies on scales as small as a few parsecs or less (e.g. Zweibel 1999). The field intensity of both components is estimated to be about 2 μG (Heiles 1996). The Zeeman measurements of magnetic field are found in the range of 7 to 16 μG (Crutcher 1999) in dark clouds, 3 to 12 μG in diffuse clouds (Myers et al. 1995; Heiles 1997), and 14 to 3100 μG in regions of massive star formation (Crutcher 1999). Also, strong magnetic fields are observed in shocks associated with expanding interstellar shells, such as the Eridanus shell (Heiles 1987). The polarization data available for some dark clouds show that the field is roughly oriented perpendicular to the projected cloud elongation (Heyer et al. 1987; Strom et al. 1988). However, in other dark clouds, the field direction is roughly parallel to the dense filaments (Vrba et al. 1976; Vrba et al. 1988). Finally, for same regions such as R CrA cloud, much more chaotic magnetic fields are observed (Vrba et al. 1981).

In this paper, we investigate the collision between two identical magnetized clouds, using a three-dimensional smoothed particle magnetohydrodynamics (SPMHD) code. The clouds are initially an intermediate stage between homogeneous and isothermal gas distribution. We considered only supersonic collisions, which are the most common case in the interstellar medium (Spitzer 1978). We focused our attention on head-on collisions because they were the only case where dense clumps were formed in previous hydrodynamics calculations (Marinho & Lépine 2000, hereafter Paper I). Two extreme field orientations were adopted: parallel and perpendicular to the relative motion of the clouds. The primary motivation of this paper is to investigate the three-dimensional effects of the magnetic field on the dynamics of cloud-cloud collision, so that we can compare the present results with the analogous non-magnetic case (Paper I).

2. Numerical methods

The present model for self-gravitating clouds motion is governed by the compressible MHD equations, where the displacement current and the effects of electrical resistivity, as well as separation of ions and electrons, are neglected. This can be reduced to the following Lagrangian equations:

$$\dot{\rho} = -\rho \boldsymbol{\nabla} \cdot \boldsymbol{v}, \tag{1}$$

$$\dot{\boldsymbol{v}} = -\frac{\boldsymbol{\nabla} \cdot \boldsymbol{\mathcal{P}}}{\rho} - \boldsymbol{\nabla}\Phi, \tag{2}$$

$$\dot{\boldsymbol{B}} = \boldsymbol{B} \cdot \boldsymbol{\nabla}\boldsymbol{v} - \boldsymbol{B}\boldsymbol{\nabla} \cdot \boldsymbol{v}, \tag{3}$$

$$\dot{u} = -\frac{p}{\rho}\boldsymbol{\nabla} \cdot \boldsymbol{v} - \mathcal{L}, \tag{4}$$

where $\boldsymbol{\mathcal{P}}$ is the negative-definite stress tensor,

$$\boldsymbol{\mathcal{P}} = \left(p + \frac{B^2}{8\pi}\right)\boldsymbol{\mathcal{I}} - \frac{\boldsymbol{B}\boldsymbol{B}}{4\pi}, \tag{5}$$

$\boldsymbol{\mathcal{I}}$ is the *three dimensional unity tensor*, $\mathcal{L}$ is the energy loss term, and Φ is the self-gravitational potential that is calculated by the Barnes & Hut (1986) tree method.

Equation (1) is not necessarily used along with the integration scheme since densities only depend on particles positions by means of the nearest neighbor searching scheme (NNS), as described in Paper I. Thus, updating positions is equivalent to update densities. Regarding time saving, it may be useful to minimize the number of NNS-calls on predicting the smoothing lengths by explicitly integrating Eq. (1) (see Paper I and references therein).

One important plasma kinematic information is the vorticity vector

$$\boldsymbol{\omega} = \boldsymbol{\nabla} \times \boldsymbol{v}, \tag{6}$$

which expresses the local fluid rotation rate, and it is connected with the magnetic field by means of the magnetic induction, Eq. (3), which can be written as (e.g., Polygiannakis & Moussas 1999)

$$\dot{\boldsymbol{B}} = (\boldsymbol{\mathcal{D}} - \boldsymbol{\nabla} \cdot \boldsymbol{v}\boldsymbol{\mathcal{I}}) \cdot \boldsymbol{B} + \frac{1}{2}\boldsymbol{\omega} \times \boldsymbol{B}, \tag{7}$$

with $\boldsymbol{\mathcal{D}} = (\boldsymbol{\nabla}\boldsymbol{v} + (\boldsymbol{\nabla}\boldsymbol{v})^{\mathrm{T}})/2$ being the *strain-rate* tensor.

The term $\frac{1}{2}\boldsymbol{\omega} \times \boldsymbol{B}$ causes the magnetic field to wind about the vorticity vector, but does not affect its magnitude. On the other hand, the term $(\boldsymbol{\mathcal{D}} - \boldsymbol{\nabla}\cdot \boldsymbol{v}\,\boldsymbol{\mathcal{I}})\cdot \boldsymbol{B}$ causes an exponential magnetic-field increase under gas compression, or decrease under gas expansion. In fact, for t much smaller than the typical time scales, the field magnitude grows as $\exp(-\frac{2}{3}\boldsymbol{\nabla}\cdot v\,t)$ if only the term $(\boldsymbol{\mathcal{D}} - \boldsymbol{\nabla}\cdot \boldsymbol{v}\,\boldsymbol{\mathcal{I}})\cdot \boldsymbol{B}$ is taken into account.

Analogously, the plasma forces can affect the vorticity in a similar way as in Eq. (7). With some algebra, extracting the curl from both sides of Eq. (2), we have the vorticity rate given by

$$\dot{\boldsymbol{\omega}} = (\boldsymbol{\mathcal{D}} - \boldsymbol{\nabla}\cdot \boldsymbol{v}\,\boldsymbol{\mathcal{I}})\cdot \boldsymbol{\omega} + \boldsymbol{\nabla}\times(\boldsymbol{f}/\rho), \tag{8}$$

where $\boldsymbol{f}/\rho$ is the right-hand side of Eq. (2).

The term $\boldsymbol{\nabla}\times(\boldsymbol{f}/\rho)$ is much more complex than the term $\frac{1}{2}\boldsymbol{\omega} \times \boldsymbol{B}$ in Eq. (7). However, we can affirm that the term $(\boldsymbol{\mathcal{D}} - \boldsymbol{\nabla}\cdot \boldsymbol{v}\,\boldsymbol{\mathcal{I}})\cdot \boldsymbol{\omega}$ causes an exponential vorticity increase or decrease analogous to the magnetic field case.

The smoothed particle magnetohydrodynamics (SPMHD) equations are derived in the usual approach of writing symmetrically the smoothed particle gradient (divergence and curl) in order to allow momentum conservation (see, e.g., Monaghan 1992 for a review).

We adopted a symmetrized form of the B-spline kernel as in Paper I. The smoothing lengths are spherically defined by means of the octal-tree based on NNS (see Paper I and references therein).

We define the following tensor:

$$\boldsymbol{\mathcal{Q}}_{ij} = \frac{\boldsymbol{\mathcal{P}}_i}{\rho_i^2} + \frac{\boldsymbol{\mathcal{P}}_j}{\rho_j^2} + \Pi_{ij}\,\boldsymbol{\mathcal{I}}, \tag{9}$$

where

$$\boldsymbol{\mathcal{P}}_i = \left(p_i + \frac{B_i^2}{8\pi}\right)\boldsymbol{\mathcal{I}} - \frac{\boldsymbol{B}_i\boldsymbol{B}_i}{4\pi} \tag{10}$$

and Π_{ij} is the pairwise artificial-viscosity coefficient (e.g., Monaghan 1992). SPH densities, ρ_i, are estimated by the traditional approach (see, e.g., Monaghan 1992).

Equation (9) is quite useful for notation saving and also it allows the modularity used in our MHD subroutines.

The artificial-viscosity coefficient Π_{ij} is written to reproduce Alfvénic shocks in the stability limit of the time integrator. Analogously to the Monaghan & Gingold (1983) artificial viscosity, we defined the SPMHD artificial viscosity as

$$\Pi_{ij} = \begin{cases} \frac{\alpha\bar{c}_{ij}\mu_{ij} + \beta\mu_{ij}^2}{\bar{\rho}_{ij}}, & \text{if } \boldsymbol{v}_{ij}\cdot\boldsymbol{r}_{ij} < 0, \\ 0, & \text{otherwise,} \end{cases} \tag{11}$$

where

$$\mu_{ij} = -\frac{\boldsymbol{v}_{ij}\cdot\boldsymbol{r}_{ij}}{\bar{h}_{ij}}\frac{1}{r_{ij}^2/\bar{h}_{ij}^2 + \eta^2} \tag{12}$$

and the coefficient $\bar{c}_{ij}$ is defined as

$$\bar{c}_{ij} = \left[\bar{s}_{ij}^2 + \frac{|\bar{\boldsymbol{B}}_{ij}|^2 - \left(\bar{\boldsymbol{B}}_{ij}\cdot\boldsymbol{v}_{ij}/|\boldsymbol{v}_{ij}|\right)^2}{4\pi\bar{\rho}_{ij}}\right]^{1/2}. \tag{13}$$

As in other works (e.g., Hernquist & Katz 1989), the following convention, $\bar{a}_{ij} \equiv 0.5(a_i + a_j)$ and $a_{ij} \equiv a_i - a_j$, is used in Eqs. (11)–(13).

The term $\bar{s}_{ij}$ in the right-hand side of Eq. (13) is the mean adiabatic sound speed for particles i and j respectively, and the magnetic term resembles the square of the Alfvén speed $v_{\rm A}^2$, but it equals zero for particles with relative velocity $\boldsymbol{v}_{ij}$ parallel to the mean magnetic field $\bar{\boldsymbol{B}}_{ij}$, and it is maximum for particles with relative velocity $\boldsymbol{v}_{ij}$ perpendicular to the mean magnetic field $\bar{\boldsymbol{B}}_{ij}$.

The SPMHD equations are given by

$$\dot{\boldsymbol{v}}_i = -\sum_j m_j \boldsymbol{\mathcal{Q}}_{ij}\cdot\boldsymbol{\nabla}W_{ij} - (\boldsymbol{\nabla}\Phi)_i, \tag{14}$$

$$\dot{\boldsymbol{B}}_i = \frac{1}{\rho_i}\sum_j m_j[\boldsymbol{B}_i\cdot(\boldsymbol{v}_j - \boldsymbol{v}_i)]\boldsymbol{\nabla}_i W_{ij}$$

$$-\frac{1}{\rho_i}\boldsymbol{B}_i\left[\sum_j m_j(\boldsymbol{v}_j - \boldsymbol{v}_i)\cdot\boldsymbol{\nabla}_i W_{ij}\right], \tag{15}$$

$$\dot{u}_i = \frac{1}{2}\sum_j m_j\,P_{ij}\,\boldsymbol{v}_{ij}\cdot\boldsymbol{\nabla}_i W_{ij} - \mathcal{L}_i, \tag{16}$$

where

$$P_{ij} = \frac{p_i}{\rho_i^2} + \frac{p_j}{\rho_j^2} + \Pi_{ij}. \tag{17}$$

The SPH-vorticity vector, $\boldsymbol{\omega}_i$, is calculated from the interpolated curl (see, e.g., Monaghan 1992):

$$\boldsymbol{\omega}_i = \frac{1}{\rho_i}\sum_j m_j\boldsymbol{\nabla}_i W_{ij}\times(\boldsymbol{v}_j - \boldsymbol{v}_i). \tag{18}$$

Equations (14)–(16) can be easily adapted to the integration scheme as described in Paper I.

3. Experiment description

As in Paper I, the physical scales $[l] = 1$ pc, $[t] = 1$ Myr, $[m] = 222.25\ M_\odot$, were chosen to normalize the gravity constant: $G = 1\ [m]^{-1}\,[l]^3\,[t]^{-2}$. The velocity unit is approximately 1 km s^{-1}. In these scales the magnetic field unit is approximately $[B] = 12\ \mu$G. Other derived physical scales were energy $[e] = 4.230\times10^{45}$ erg, power $[\dot{e}] = 1.340\times10^{38}$ erg s^{-1}, and density $[\rho] = 1.505\times10^{-20}$ g cm^{-3}.

Similarly to Paper I, our interstellar cloud model consists of a mixture of atomic and molecular hydrogen, helium and traces of CO. Initially, the clouds have a temperature of approximately 20 K. The cooling and the heating mechanisms are the same as in Paper I, as well as the adopted chemical model for H and H_2 balance, which reflects a strong nonlinear dependency of the specific thermal energy on density and temperature. We refer the reader to Paper I for further details concerning the thermal and chemical models.

The simulation starts by impinging two identical spherical clouds onto each other at a supersonic relative speed of approximately 10 km s^{-1}. Both clouds have an

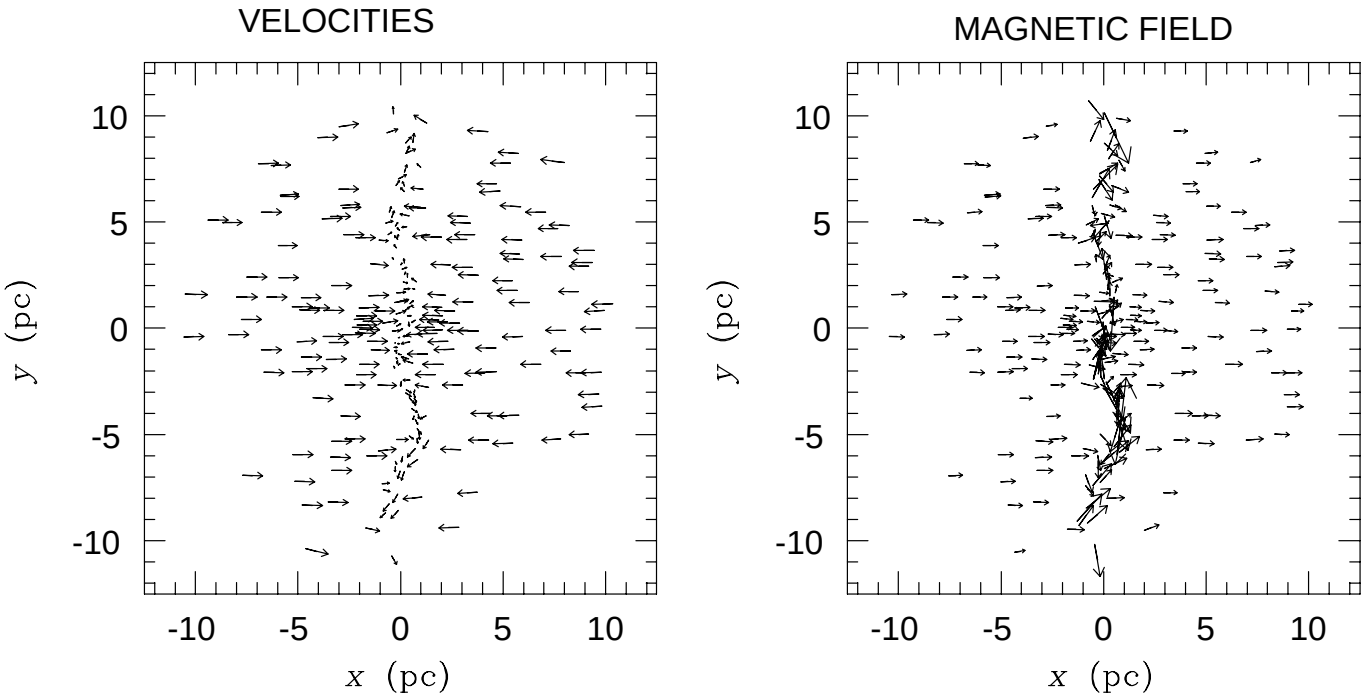

Fig. 1. Velocity (left panel) and magnetic field (right panel) configurations of a $z = 0$ slice with 0.5 pc in thickness at $t = 1.5$ Myr in the parallel case. The arrows indicate the field direction and the length is proportional to the field's magnitude.

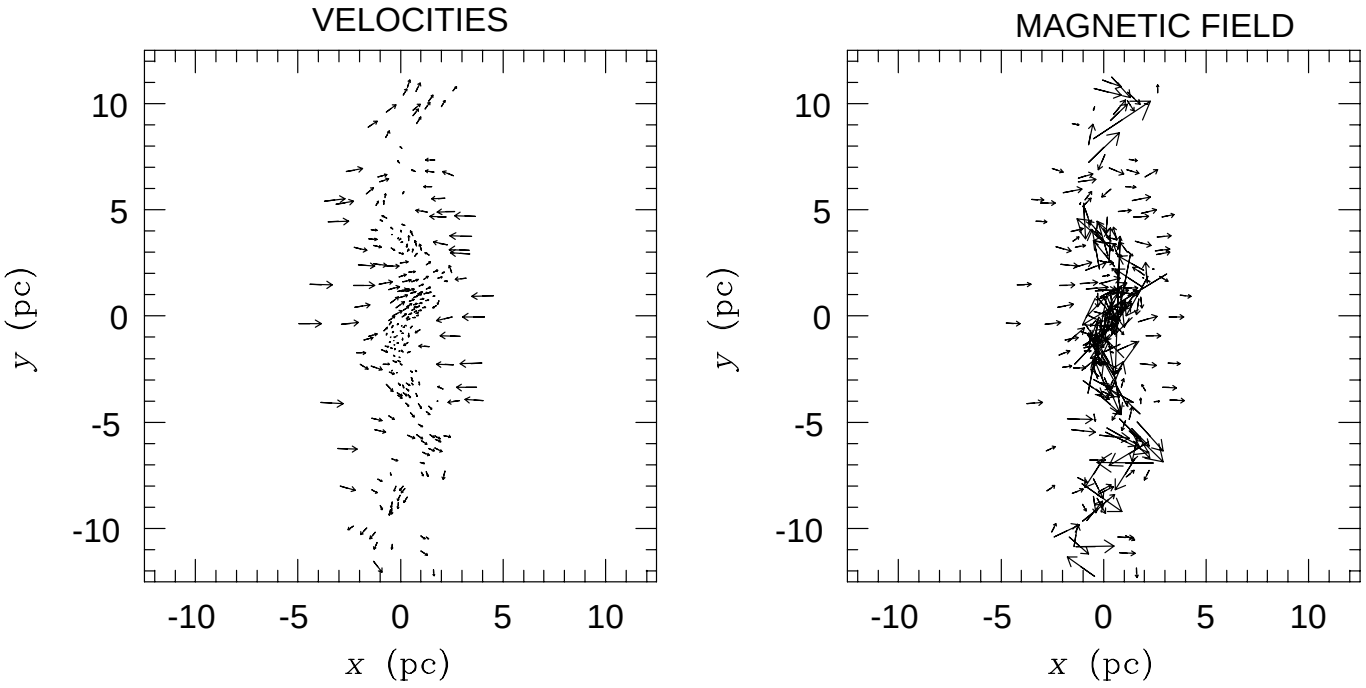

Fig. 2. The same as in Fig. 1 but at $t = 2.5$ Myr.

initial mass of $M = 2222.5\ M_\odot$, a temperature $T = 20$ K, and a cut-off radius $R_c = 10$ pc. Each cloud contains 4096 particles initially distributed by Monte Carlo, according to the density law

$$\rho(r) = \frac{M}{2\pi {R_c}^2} r^{-1}. \tag{19}$$

The mean adiabatic sound-speed and the Alfvén speed are approximately $s = 3.2 \times 10^4$ cm s^{-1} and $v_A = 2.6 \times 10^5$ cm s^{-1}, respectively. These values allow a supersonic shock with Mach numbers $\mathcal{M} = v/s = 62$ and $\mathcal{M}_B = v/v_A = 3.8$, respectively.

In present work, we performed only simulations for the head-on case. For the same initial conditions as in Paper I, we set up two distinct experiments, labeled by the initial magnetic field orientation: *parallel* and *perpendicular* to the initial clouds motion. The magnetic field is initially

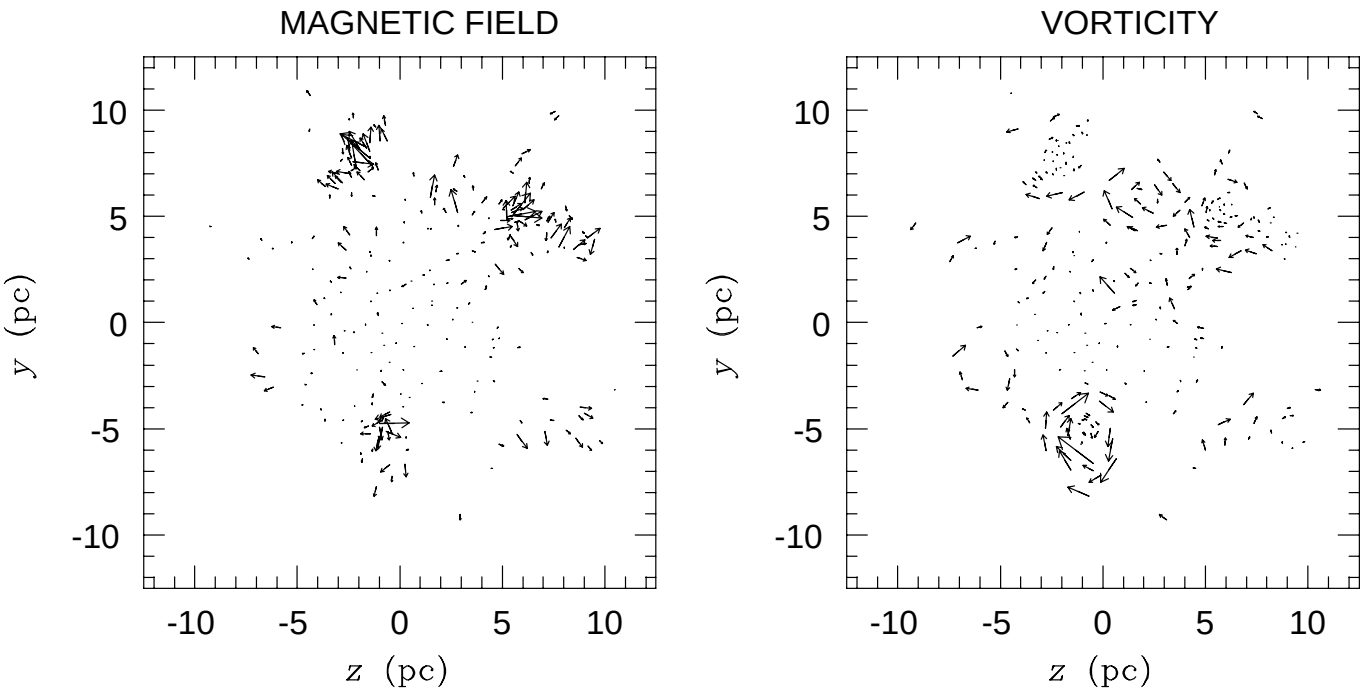

Fig. 3. The zy-projection of the magnetic field $\boldsymbol{B}$ (left panel) inside an $x = 3$ pc slice with 0.5 pc in thickness, and the SPH vorticity $\langle \boldsymbol{\nabla} \times \boldsymbol{v} \rangle$ (right panel) at $t = 2.5$ Myr in the parallel case.

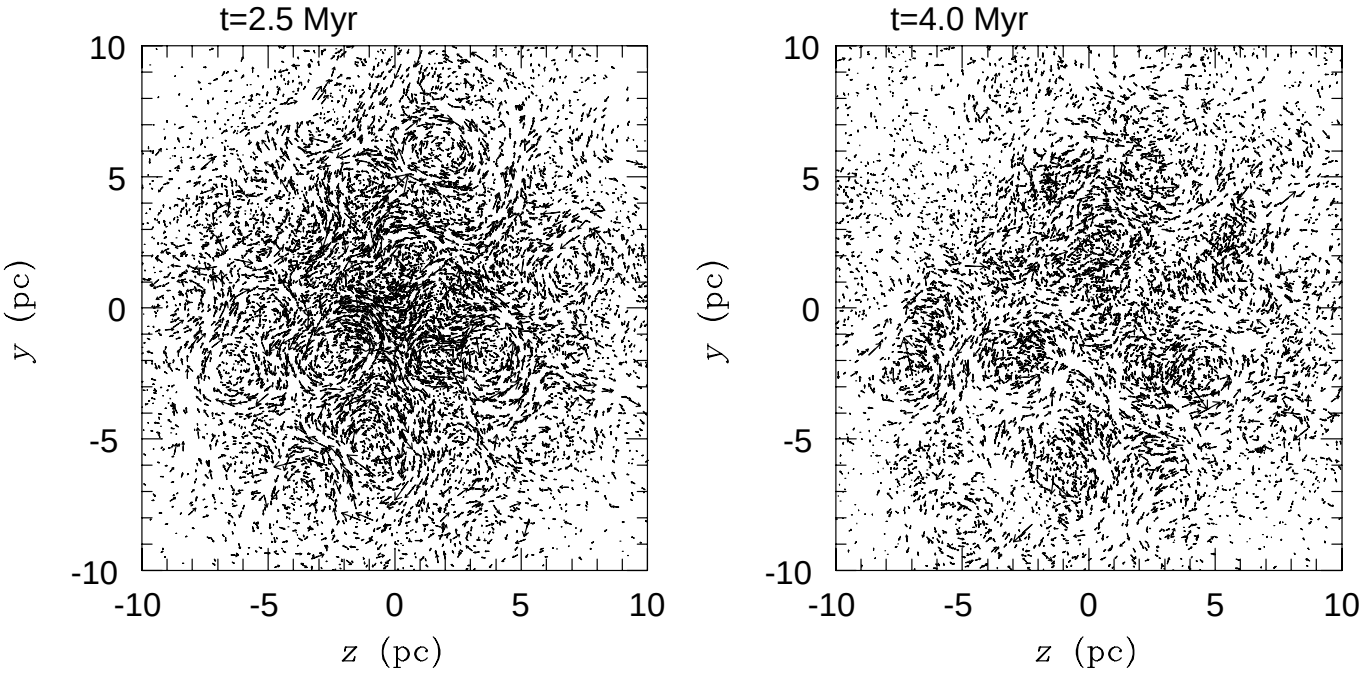

Fig. 4. The SPH vorticity projected onto the zy-plane at $t = 2.5$ Myr (left panel) and $t = 4.0$ Myr (right panel), respectively, in the parallel case.

homogeneous, and we adopted an initial strength of 12 μG based on typical values observed in dark molecular clouds.

The code parameters were $\epsilon_{\rm max} = 0.5$, $\epsilon_{\rm min} = 0.05$, $\theta = 0.25$, $\Delta t_0 = 0.0078125$, $N_f = 48 \pm 2$, $\alpha = 3$, $\beta = 5$, $\eta^2 = 0.01$, and 8 time-bins were used in the integration scheme, allowing a minimum time-step of $\Delta t_7 \approx 6.1 \times 10^{-5}$. These values were based on accuracy/stability considerations discussed in Paper I.

As in Paper I, the cloud models were not initially in hydrostatic equilibrium. However, the time scales involved in the internal cloud motions were one order of magnitude larger than that of the main term of the collision process, so that we could assume that the relaxation effects were small compared to the effects caused by the shock itself. If we allowed the initial clouds to relax (under the imposed environment) before the collision experiment

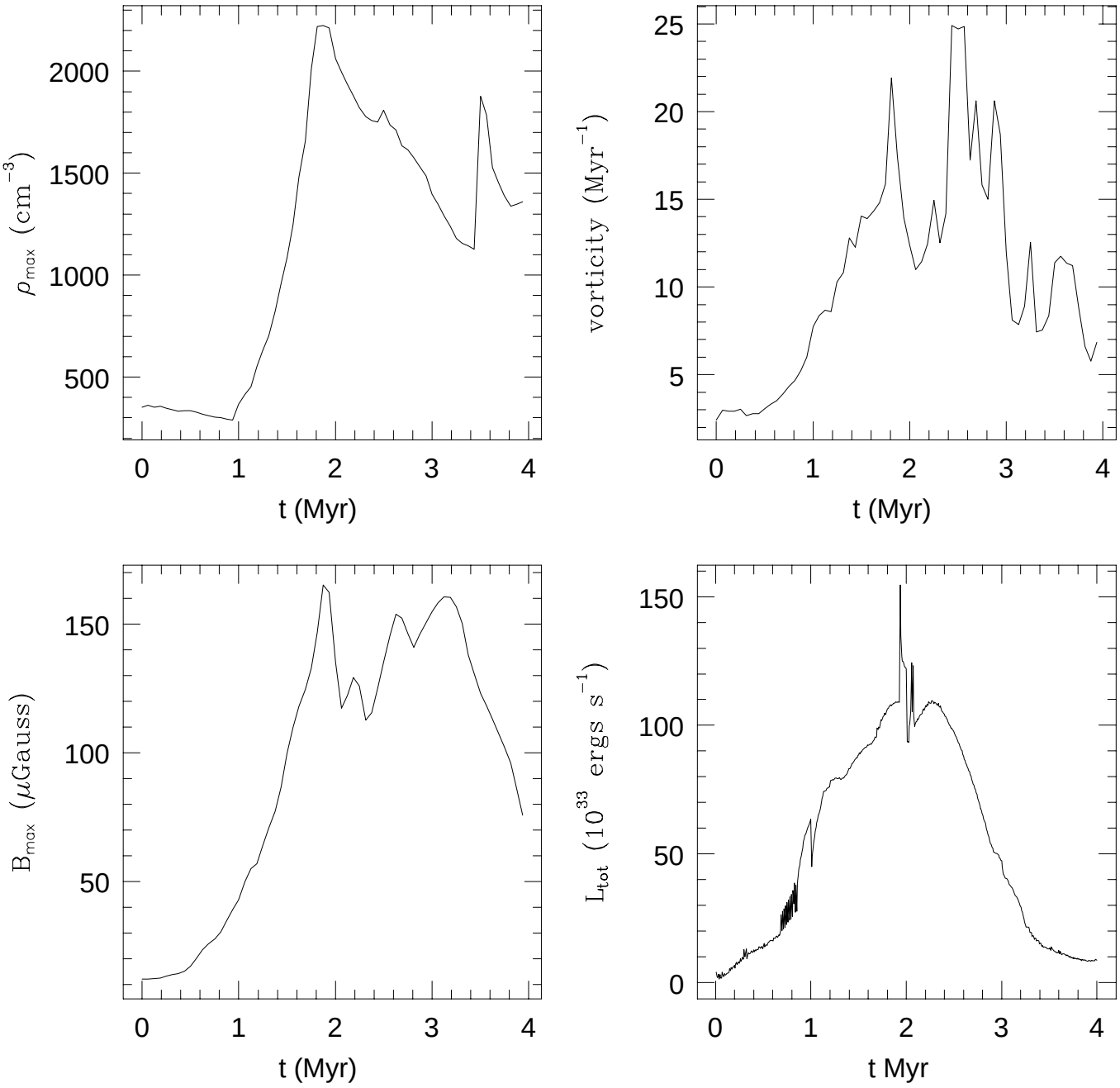

Fig. 5. The evolution (parallel case) of the maximum values for density (H cm^{-3}), vorticity (Myr^{-1}), magnetic field (μG), respectively, and the evolution of the energy-loss rate (10^{33} erg s^{-1}).

starts, our clouds would never reach the hydrostatic balance since the involved processes are dissipative and interact with the magnetic field under the MHD approximation. On the other hand, if we setup the initial conditions for adiabatic hydrostatic equilibrium, as we switch on the cooling-heating mechanisms, and also the magnetic field, the clouds assume a non-equilibrium configuration with a similar behavior to the initial conditions adopted in present work.

Our definition for clump is somewhat arbitrary and has a geometrical basis. Our algorithm uses a list of SPH particles sorted according to their densities to promote the densest particle (with density ρ_c) to the *clump core*, and removes it from the list. For this particle (clump core), the algorithm searches for the nearest neighbors satisfying the condition $\rho \geq 0.5\rho_c$. Each neighbor obeying the latter condition is promoted to a *clump member*, and then removed from the list to avoid overcounting and clump overlap. We do not know where a clump ends but where its density drops to half the peak.

To avoid statistical fluctuations being classified as clumps, we have introduced in the clump analysis a "*floor condition*" to reject clump core candidates with densities lower than the $\bar{\rho} + 2\,\sigma_\rho$ threshold, where σ_ρ is the density

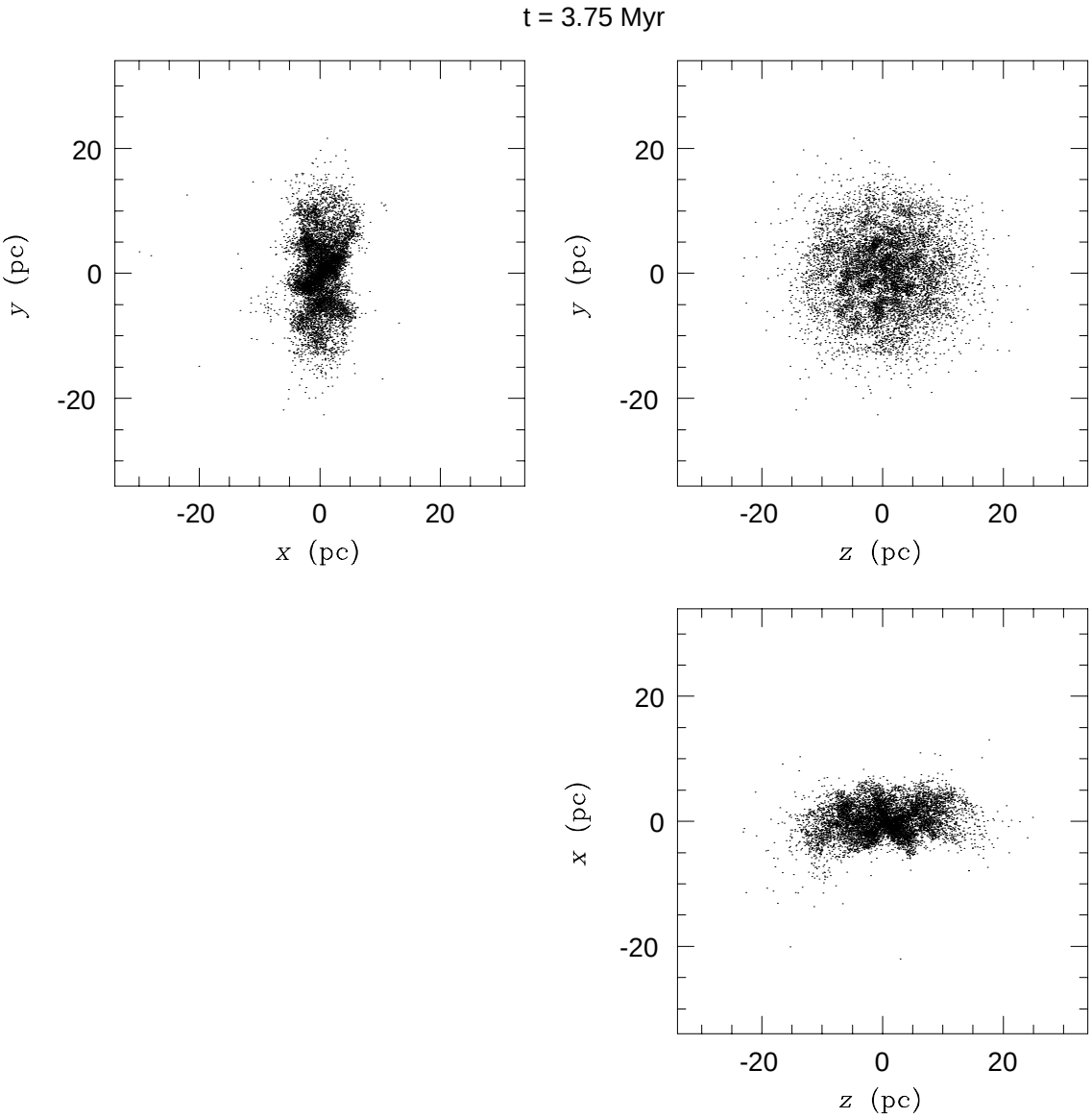

Fig. 6. The collision debris of the parallel case at $t = 3.75$ Myr. This figure reveals more clearly the clumped structure of the remnants.

dispersion. Without this condition, a Monte Carlo generated homogeneous sphere would be entirely recognized as one single clump. Thus, what we consider to be a real clump is a density enhancement much above the expectation value. This procedure is repeated until the list of clump candidates becomes empty.

4. Results

4.1. Parallel case

Figures 1 and 2 illustrate the configurations for velocity and magnetic field of a $z = 0$ slice with 0.5 pc in thickness at 1.5 and 2.5 Myr, respectively. It is evident from these figures that the magnetic field was amplified in the shock layer, which was caused by the strong compression that was mentioned previously (Sect. 2). Differently from the non-magnetic case, in which the maximum compression occurred at 1.5 Myr, in present experiment the shocked clouds reached its maximum compression at about 2.5 Myr, but the maximum density peak, observed for a particle centered in the densest clump, occurred at 1.92 Myr. One possible explanation is that the magnetic field retains most of the colliding gas, unlike their hydrodynamics counterparts where the colliding gas can freely escape throughout the symmetry plane.

Figure 3 shows the configurations for the magnetic field and the vorticity inside an $x = 3$ slice with 0.5 pc in thickness at 2.5 Myr. The slice is passing through four clumps, revealed by the arrows concentration for both magnetic field and vorticity. The vorticity distribution reaches its maximum magnitude around the dense clumps. In the high-vorticity region, the magnetic field is amplified in

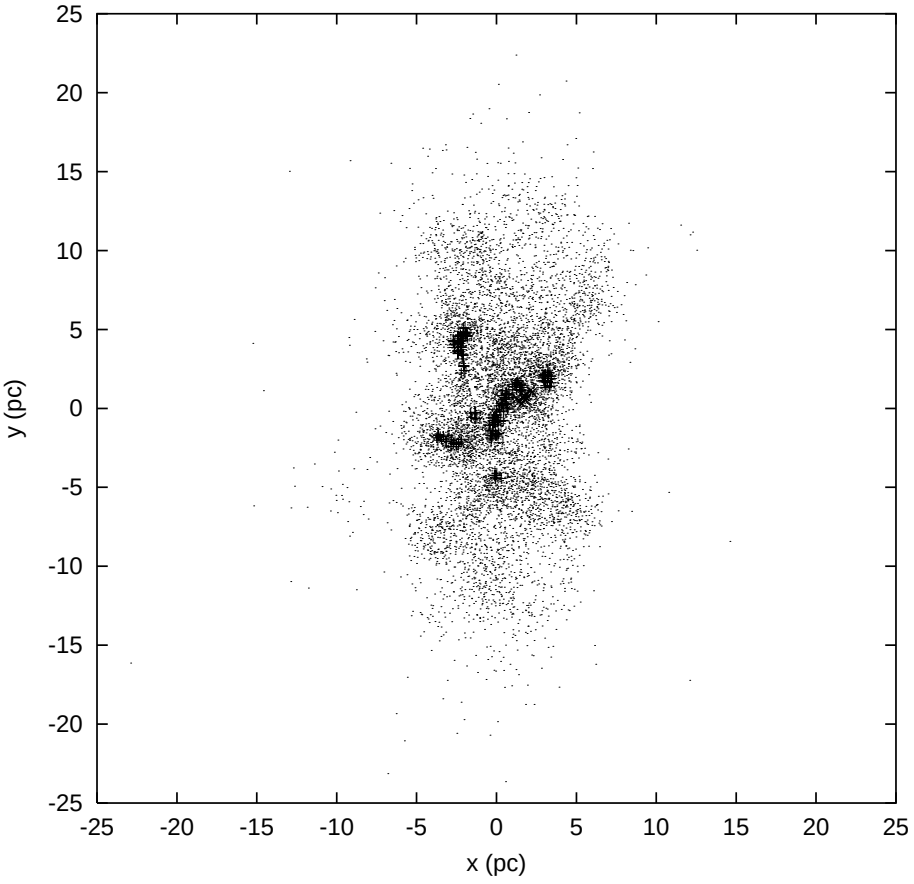

Fig. 7. A close view in the particle configuration projected onto the xy-plane at 4 Myr in the parallel case. The higher density regions ("*clumps*") are indicated by crosses.

accordance with 2D simulations of shock cloud interaction (e.g., Mac Low et al. 1994; Jones et al. 1997).

The vorticity configuration can be seen in Fig. 4 for two epochs; the plots reveal the eddies formed along with the collision, and they survived until the end of the simulation. The maximum vorticity magnitude (approximately 25 km s^{-1} pc^{-1}) at $t = 2.5$ Myr (left panel) was the maximum reached during the experiment, whereas the maximum vorticity magnitude at $t = 4.0$ Myr (right panel) was approximately 6.9 km s^{-1} pc^{-1}.

We keep track of the evolution of the quantitative properties associated to critical regions by depicting their maximum values occurred in the collision at each timestep. Figure 5 shows the evolution of the maximum values for density $\rho_{\max}$ (in H mass per cubic centimeter), vorticity magnitude $\omega_{\max}$ (in km s^{-1} pc^{-1}) and magnetic-field strength $B_{\max}$ (in μG), as well as the evolution of total luminosity $L_{\rm tot}$ (in 10^{33} ergs s^{-1}). All the plots show simultaneous local peaks around 1.95 Myr, which can be a consequence of the maximum compression reached by the clouds. At this epoch, the maximum density, the maximum magnetic field and the total luminosity reached their peak values of $\rho_{\max} \approx 2.25 \times 10^3$ cm^{-3}, $B_{\max} \approx 165$ μG, and $L_{\rm tot} \approx 155 \times 10^{33}$ ergs s^{-1}, respectively. At $t \approx 2.5$ Myr there is a local peak in density synchronized with the peak in vorticity, approximately 25 km s^{-1} pc^{-1} (the maximum value of the experiment). They might be associated to a peak near 2.6 Myr in the evolution of the maximum field strength. However, the nearest peak in the luminosity evolution occurs just before, at 2.3 Myr. There is a noticeable peak near 3.5 Myr in the evolution of the maximum density, which is perhaps physically associated with the peak at the same epoch in the evolution of the maximum vorticity. However, this peak in the maximum density evolution is preceded by a peak in the maximum magnetic field evolution near 3.2 Myr. At 4 Myr, the maximum magnetic field strength is significantly greater ($\sim$75μG) than the initial value. The luminosity-evolution profile resembles the analogous non-magnetic case but is reduced in amplitude by a factor of 1.63. Also, the peaks in the luminosity occur in 1.92 Myr in the MHD case and 1.48 Myr for the non-magnetic case.

The collision debris are shown in Fig. 6 at 3.75 Myr. This epoch is just 0.25 Myr after denser structures have formed (see Fig. 5), but they eventually dissipate. The collision remnants resemble qualitatively those shown in Paper I. However, the clumped structure shown here is much coarser than that shown in the analogous non-magnetic case (report to Fig. 5 in Paper I).

The experiment stops at 4 Myr, and the collision remnants show almost the same structures shown in Fig. 6, but with a small variation in the density peak (see Fig. 5). Using the same technique as in Paper I, we found 22 denser regions (clumps) as shown in Figs. 7 and 8. According to both figures, the clumps distribution forms elongated structures in the xy-view. The clumps have density-peaks

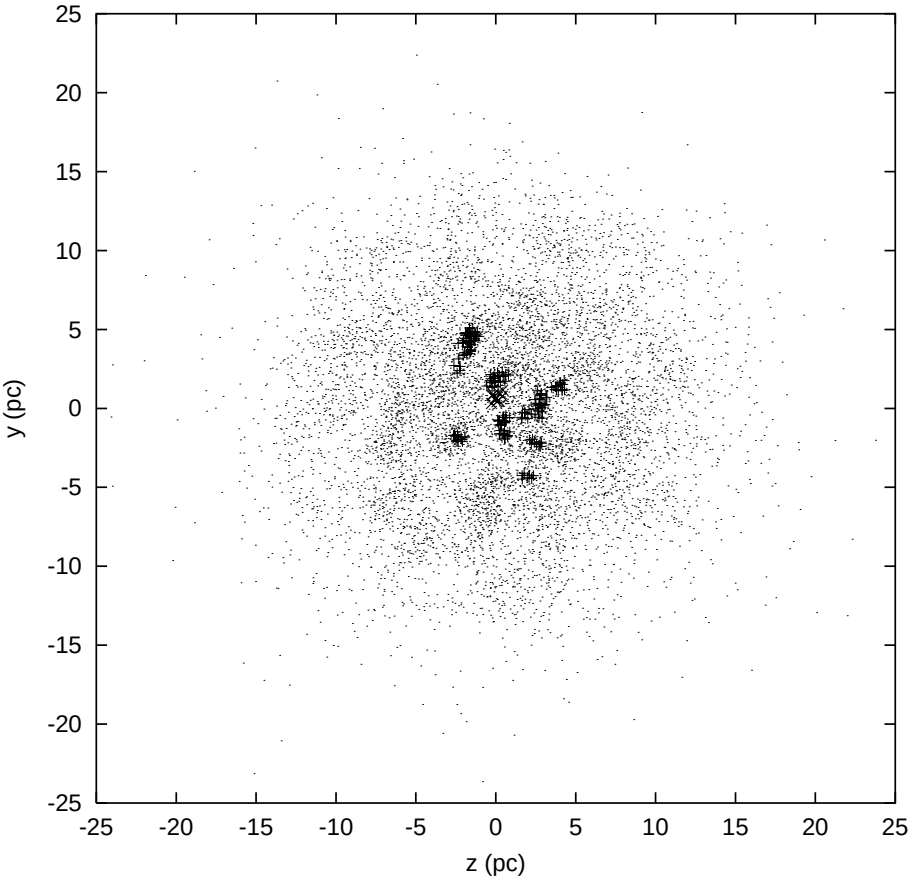

Fig. 8. As in Fig. 7 but in the zy-plane.

in the 460–1359 H cm^{-3} range. However, the average density of each clump varies from 418 through 829 H cm^{-3}. The temperature is approximately constant in the clumps and it lies in the 11.75–55.15 K range. Each clump has effective size (rms) between 0.15 pc and 0.50 pc. The denser clumps are generally the smaller and colder ones (see Fig. 9). However, the densest (coldest) clump has effective radius of 0.44 pc.

4.2. Perpendicular case

Figures 10 and 11 illustrate the configurations for velocity and magnetic field of a $z = 0$ slice with 0.5 pc in thickness at 0.9 and 1.6 Myr, respectively. The clouds are magnetically supported, so that they collapse along the field lines but not in perpendicular directions. As a consequence, the clouds become flattened (Fig. 11). The figures show that the magnetic-field strength is amplified in the accretion layer, the region in which the velocity field converges. Such a field compression forms a magnetic shield in front of both cloud that inhibits a direct contact of the clouds.

Figure 12 shows the configuration for vorticity and magnetic field of a slice with 0.5 pc in thickness at time $t = 1.9$ Myr. The vorticity configuration of both slices is shown in the left column, and the corresponding magnetic field configuration is shown in the right column. In the xz-plane (top view) a high concentration of magnetic field at position $(2, 4)$ approximately, contoured by the vorticity vectors is evident. In the yz-slice (the collision plane) there is an almost coherent vorticity stream in the negative z-direction, whereas the magnetic-field is roughly in the y-direction.

The evolutions of the maximum values for density, vorticity and magnetic field, as well as the evolution of the total luminosity, are shown in Fig. 13. As in the parallel case (Fig. 5), some synchronized maxima occurred. For instance, the evolution of the maximum-density and the maximum-vorticity have their peaks of $\rho_{\max} = 4.65 \times 10^2$ H cm^{-3} and $\omega_{\max} = 13.8$ Myr^{-1}, respectively, at about 1.8 Myr. The maximum magnetic-field evolution has a peak of $B_{\max} = 110$ μG at about 1.7 Myr. The final maximum magnetic field is about three times its initial value. The evolution of the total luminosity is quite different from the parallel case: the maximum occurred about 0.65 Myr, whereas, in previous case it occurred about 1.95 Myr. Furthermore, the total amount of energy lost was smaller than in the parallel case. The evolution of the maximum magnetic-field reveals an interesting behavior. From 2.0 Myr and after, the maximum field-strength drops off in a stepwise way, following the local peaks decay in the vorticity plot.

The collision remnants for the perpendicular case are shown in Fig. 14 at $t = 3.75$ Myr. No cloud fragmentation was observed. However, it is evident from the figure the formation of an elongated structures in the z-direction.

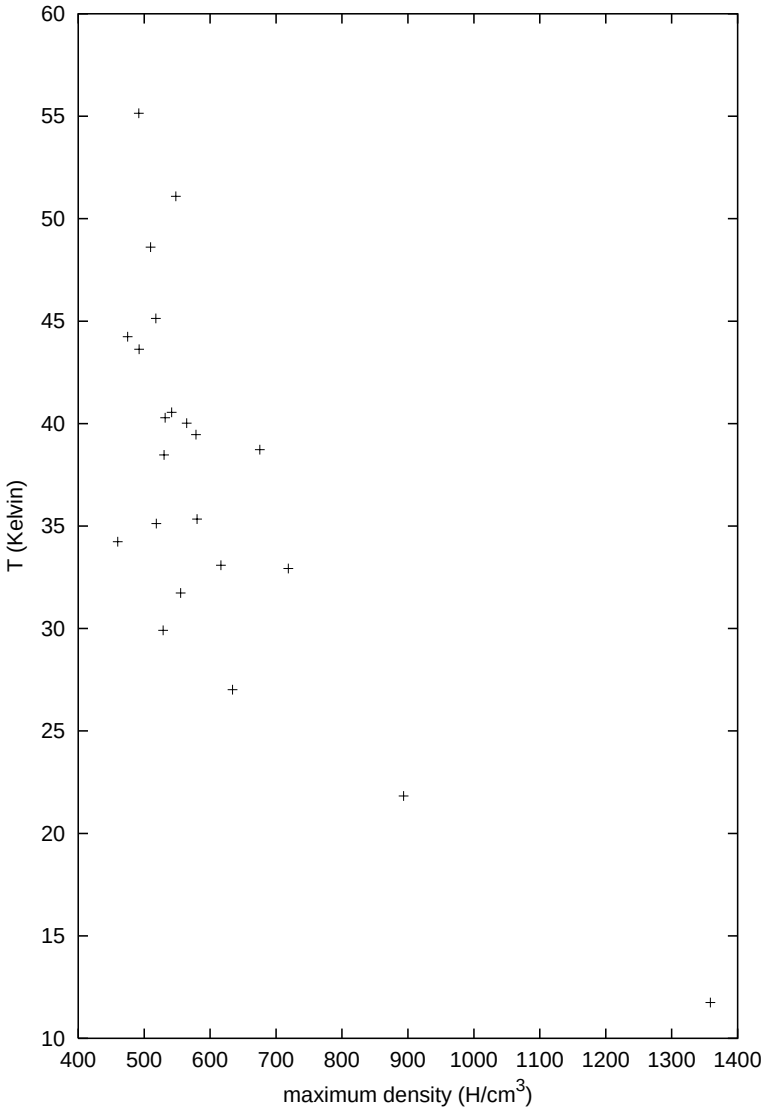

Fig. 9. Maximum density versus mean temperature in the identified clumps in the parallel case (the denser regions contoured by half the central density, as in Paper I). The plot reveals a slight correlation between central density and temperature. Denser regions are the colder ones.

Similar results were found in 2D collision between supersonic diffuse clouds by Miniati et al. (Miniati et al. 1999).

5. Discussion and conclusion

We studied two special cases of head-on supersonic collision between two identical magnetized clouds using a three-dimensional SPMHD code. In the first case, the magnetic field was initially parallel to the clouds motion, and in the second case the field was initially perpendicular. We focused on the effects of the magnetic field on the clumps formation by cloud-cloud collision. The initial conditions were the same as a previous work (Paper I) except for the presence of a homogeneous magnetic field of approximately 12 μG.

As an SPMHD innovation, we modified the Monaghan & Gingold (1983) artificial viscosity in order to reproduce magnetohydrodynamics shock. In fact, such an artificial viscosity model was crucial in the case of collision perpendicular to the magnetic field. A more detailed discussion of the present SPMHD code as well as a set of MHD tests will be presented in a future work.

The magnetic field was amplified and deformed in the shocked layer in both cases. Its magnitude reached values as higher as 160 μG and 110 μG in the parallel and in the perpendicular cases, respectively, and decayed subsequently. The field distribution seems chaotic in larger scales, however, it distributes more coherently in the clumps. Moreover, in the first 1 Myr of the parallel case the magnetic field evolved to a wiggled aspect in the shock layer but remained almost homogeneous outside the shock. The referee argued that the Monte Carlo seed density perturbations were the responsible for the wiggles shown in the present results and that they are germinated when these inhomogeneities try to smooth out before hitting the shock. This is a plausible explanation for this effect.

The presence of the magnetic field, with typical magnitudes of dark molecular clouds, affects considerably the evolution of head-on cloud-cloud collision. Strong vortices were formed in contrast to the non-magnetic case.

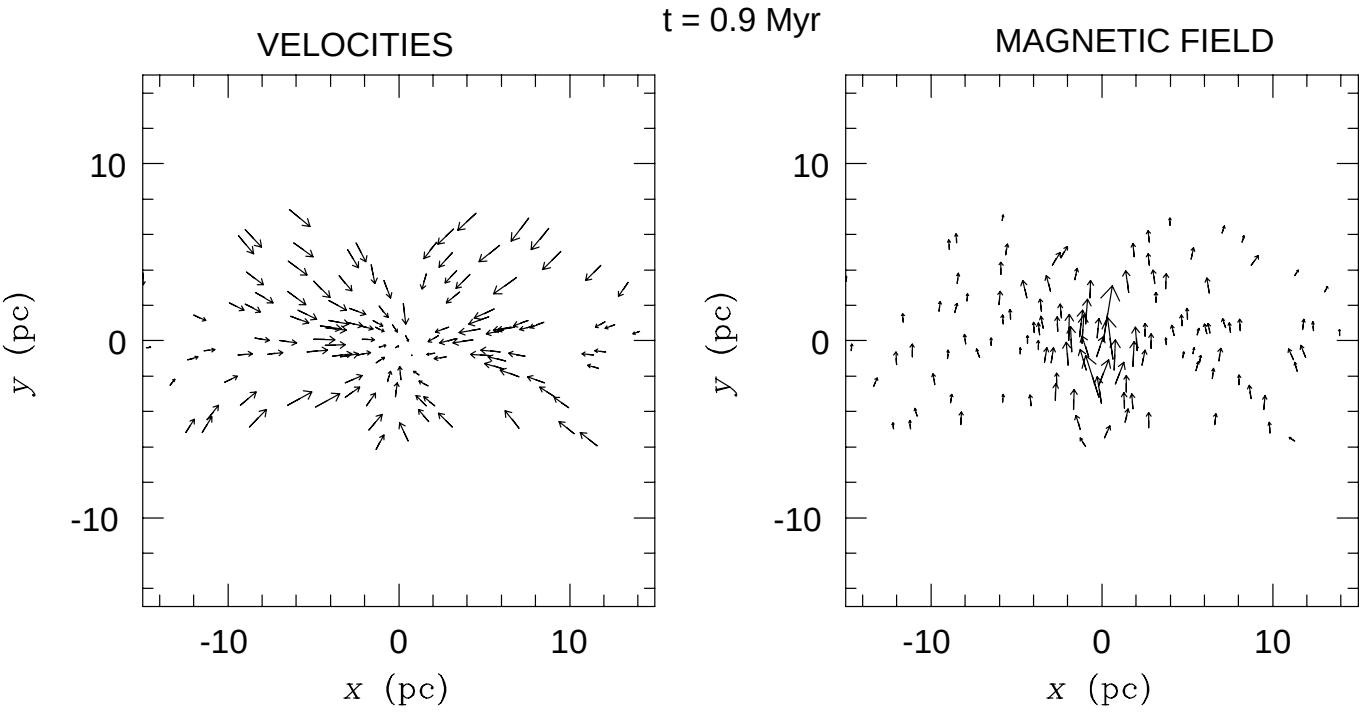

Fig. 10. From left to right, respectively, the velocity field and the magnetic field of a slice with 0.5 pc in thickness passing through $z = 0$ at $t = 0.9$ Myr in the perpendicular case.

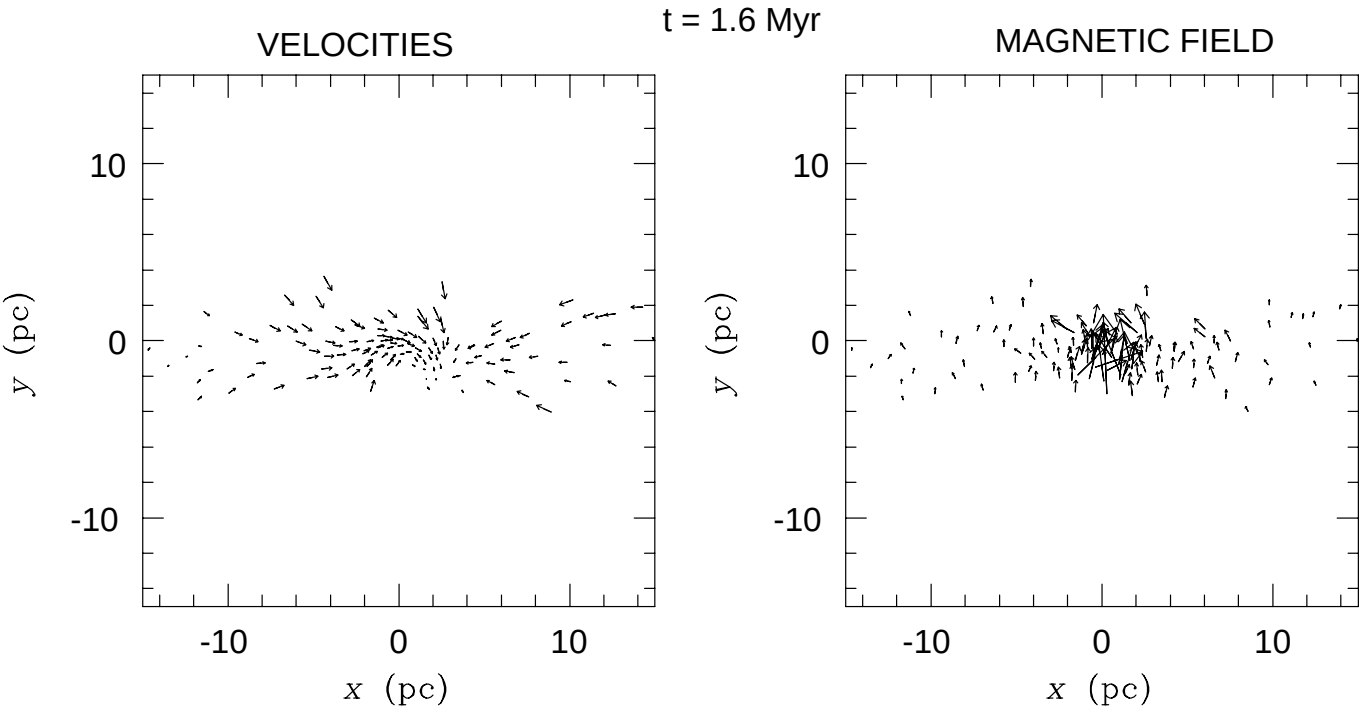

Fig. 11. As in Fig. 10 but at $t = 1.6$ Myr.

They were distributed throughout the shocked layer, and they persist until the end of the simulation. In the parallel case the vorticity distribution presents an almost regular pattern, whereas in the perpendicular case the vorticity distribution looks chaotic. Also, we noticed that the vorticity distribution contours the clumps and that its magnitude grows proportionally to the distance to the clumps mass-center, reaching its maximum at the clumps boundaries. This interesting behavior could be interpreted as the gas (particles) having a toroidal motion about the clump's mass-center. However, one plausible explanation is that the clumps are traveling along the field lines and against

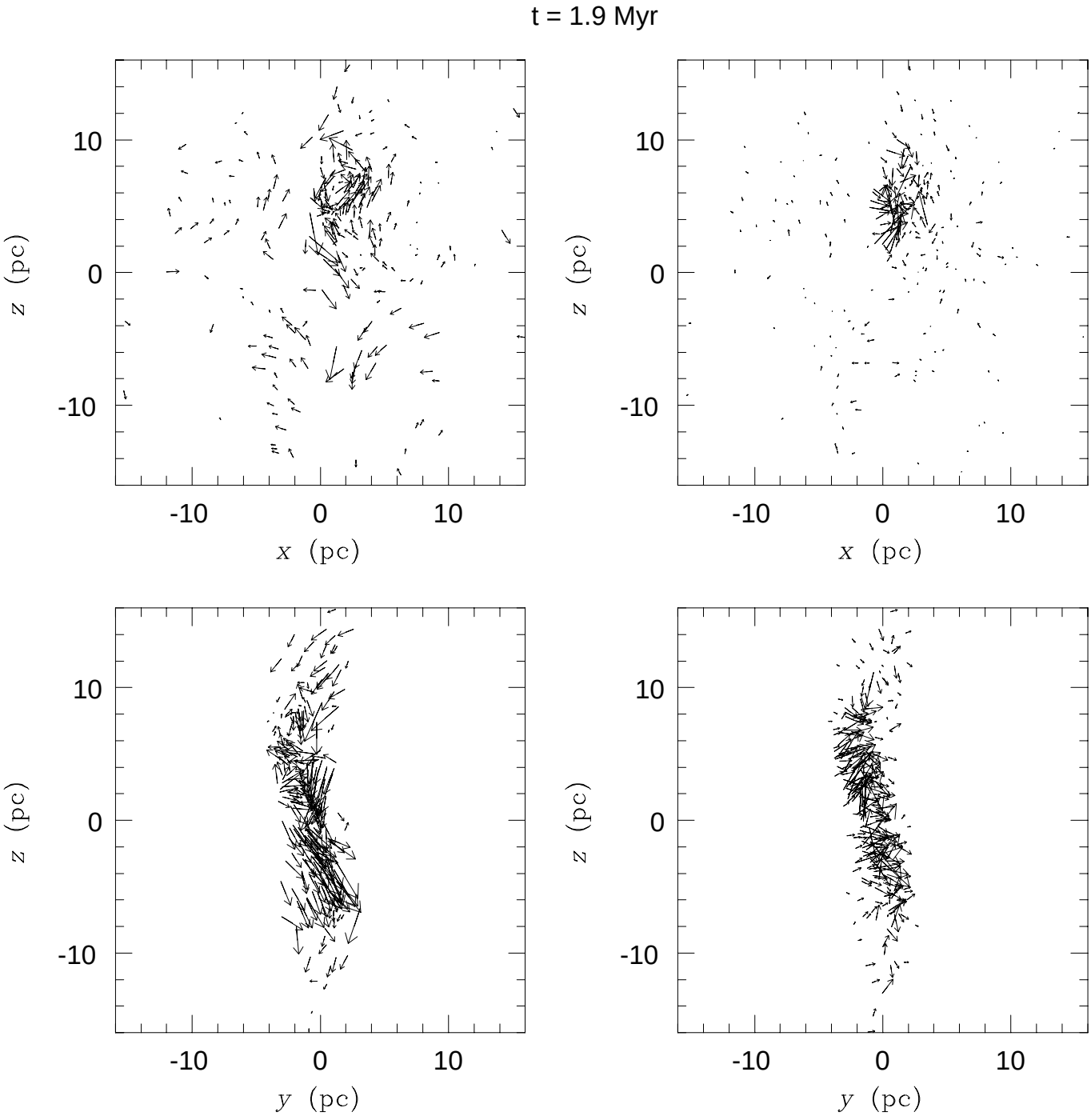

Fig. 12. Vorticity (left column) and magnetic field (right column) in two orthogonal views (xz and yz) inside a thin slice of 0.5 pc in the perpendicular case.

the low density regions. This motion may be a result of the confinement caused by the field, since in the non-magnetic case such a result did not occur.

The cloud compression was much more efficient in the parallel case than in the perpendicular one. In the former case, particles were confined by the field lines, and in the later, the field lines were compressed in the shocked layer, forming a magnetic shield that inhibits a direct contact of both clouds. In the later case, the stored magnetic pressure slowly stops the clouds and reverses their motions. Similar results were found in 2D collisions between supersonic diffuse clouds by Miniati et al. (Miniati et al. 1999).

The large-scale density distribution in the parallel case resembles the analogous non-magnetic case, but differs considerably on small scales. However, the density distribution of the perpendicular case is quite different from the non-magnetic case on all scales.

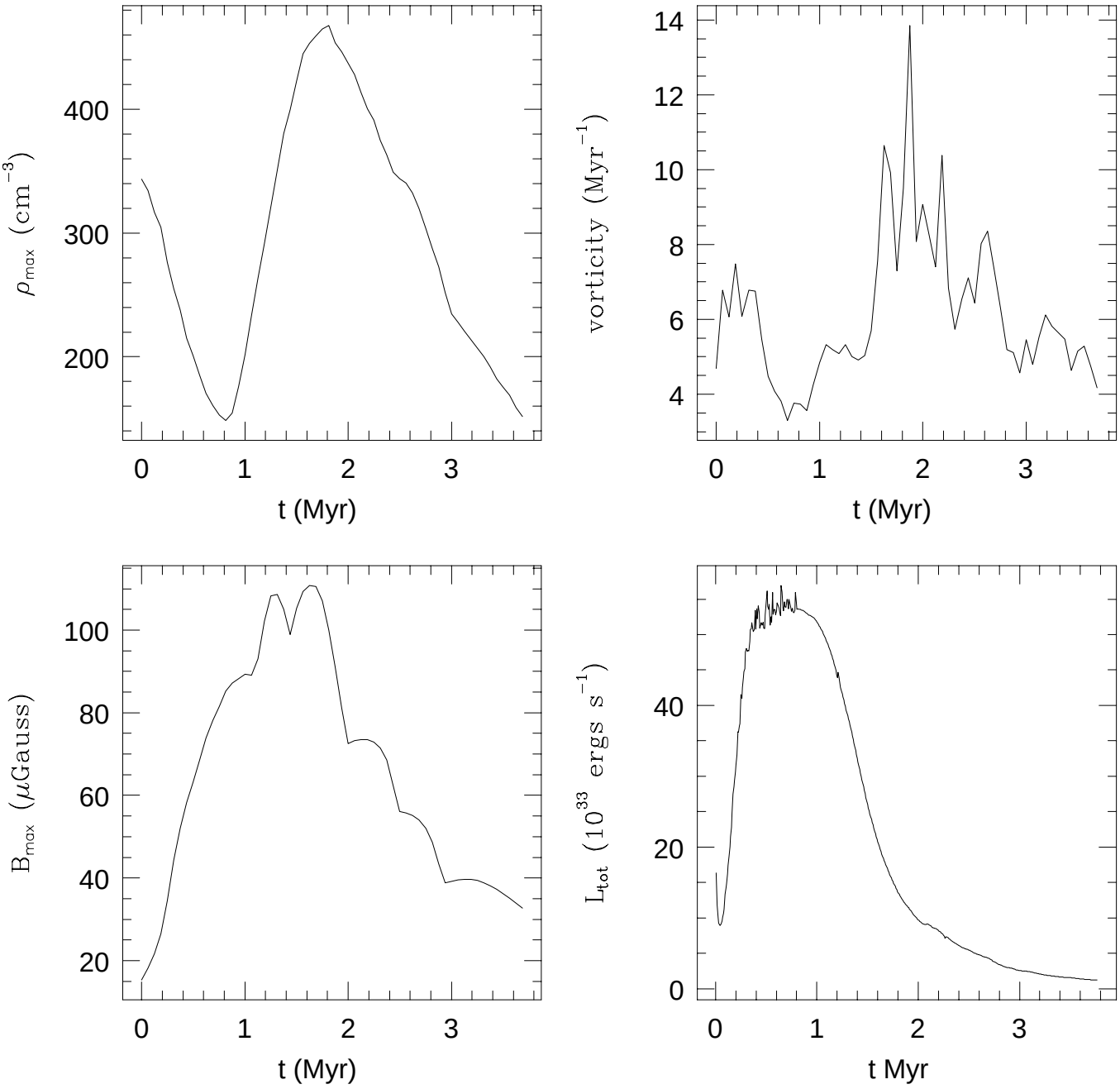

Fig. 13. As in Fig. 5 but for the perpendicular case.

The clump formation was present in the parallel case, but it was absent in the perpendicular case, or at least not detectable by the adopted definition for clump. Clumps had a population of 60−96 particles. For the chosen number of neighbors (∼48), we conclude that the formed clumps are in agreement with the resolution requirement. The 22 formed clumps contain a total of 1728 particles. However, as in Paper I, the gravity resolution was limited by the lower and upper limits for the adaptive softening length $0.05 \leq \epsilon \leq 0.5$. For regions where $h < 0.05$ the smoothing length is $h \leq \epsilon$, and then the local Jeans mass becomes larger than the minimum resolvable mass. For $h > 0.5$ the smoothing length is $\epsilon \leq h$, and then we could have artificial fragmentation but we did not have fragments greater than this upper limit. Clumps have formed preferentially in the denser parts of the collision remnants, where the local Jeans mass could be smaller than the minimum resolvable mass.

Clumps were not detected in the parallel case, nor in the off-center collision of Paper I, even if we dropped the density floor down to σ_ρ above the mean density $\bar{\rho}$. Also, we performed a collapse experiment with one cloud, with the same initial cloud model, initially at rest, and no fragments were detected. These facts suggest that

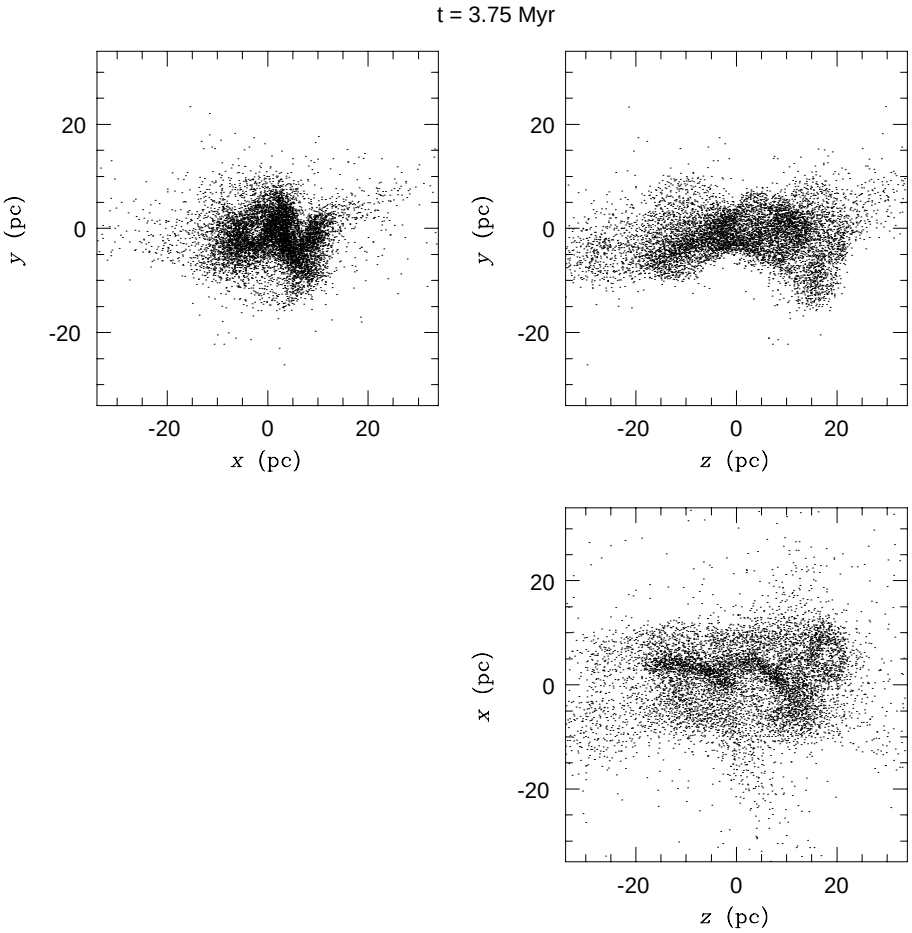

Fig. 14. The three orthogonal view of the collision debris of the perpendicular field case.

the fragments formed in present work were not endemic (Whitworth 1998) but in fact produced by the strong compression allowed by the special field orientation (parallel to the initial motion) combined with the efficient cooling.

The presence of magnetic field just retarded the fragmentation process and allowed the formation of larger and hotter clumps than in the non-magnetic case. For instance, in the previous work we found clumps as dense as 10^4 H cm^{-3}, most of them with sizes of the order of 10^{-1} pc and temperatures in the 11–20 K range. In present work, we found clumps with densities of the order of 10^3 H cm^{-3}, most of them with sizes ranging 0.3–0.5 pc and temperatures in the 25–50 K range.

Acknowledgements. We are grateful to Anthony Whitworth, the referee, for useful comments and suggestions. E.P.M. and C.M.A. are thankful to FAPESP for the financial support. This research has made use of NASA's Astrophysics Data System (ADS) Bibliographic Services.

References

Barnes, J. E., & Hut, P. 1986, Nature, 324, 446
Buckley, H. D., & Ward-Thompson, D. 1996, MNRAS, 281, 294
Clifford, P., & Elmegreen, B. G. 1983, MNRAS, 202, 629
Crutcher, R. M. 1999, ApJ, 520, 706
Elmegreen, B. G. 1988, ApJ, 326, 616
Gilden, D. L. 1984, ApJ, 279, 335
Habe, A., & Ohta, K. 1992, PASJ, 44, 203
Hasegawa, T., Sato, F., Whiteoak, J. B., & Miyawaki, R. 1994, ApJ, 429, L77
Hausman, M. A. 1981, ApJ, 245, 72
Heiles, C. 1987, in Interstellar Processes, ed. D. J. Hollenbach, & H. A. Jr. Thronson (Dordrecht:Reidel), 171
Heiles, C. 1996, in Polarimetry of the Interstellar Medium, ed. W. G. Roberge, & D. C. B. Whittet (San Francisco: ASP), PASP Conf. Ser. 97, 457
Heiles, C. 1997, ApJS, 111, 245
Hernquist, L., & Katz, N. 1989, ApJS, 70, 419
Heyer, M., Vrba, F. J., Snell, R. L., et al. 1987, ApJ, 321, 855
Jones, T. W., Gaalaas, J. B., Ryu, D., & Frank, A. 1997, ApJ, 482, 230
Keto, E. R., & Lattanzio, J. C. 1989, ApJ, 346, 184
Kimura, K., & Tosa, M. 1996, A&A, 308, 979
Klein, R. I., & Woods, D. T. 1998, ApJ, 497, 777
Lattanzio, J. C., Monaghan, J. J., Pongracic, H., & Schwarz, M. P. 1985, MNRAS, 215, 125
Little, L. T., Riley, P. W., Macdonald, G. H., & Matheson, D. N. 1978, MNRAS, 183, 805
Loren, R. B. 1976, ApJ, 209, 466
Mac Low, M.-M., McKee, C. F., & Klein, R. I, 1994, ApJ, 433, 757
Marinho, E. P., & Lépine, J. R. D. 2000, A&AS, 142, 165 (Paper I)
Meyerdierks, H. 1992, A&A, 253, 515
Miniati, F., Jones, T. W., Ferrara, A., & Ryu, D. 1997, ApJ, 491, 216

Miniati, F., Ryu, D., Ferrara, A., & Jones, T. W. 1999, ApJ, 510, 726
Miyawaki, R., Hayashi, M., & Hasegawa, T. 1986, ApJ, 305, 353
Monaghan, J. J. 1992, ARA&A, 30, 543
Monaghan, J. J., & Gingold, R. A. 1983. J. Comput. Phys., 52, 374
Myers, P. C., Goodman, A. A., Güsten, R., & Heiles, C. 1995, ApJ, 442, 177
Odenwald, S., Fischer, J., Lockman, F. J., & Stemwedel, S. 1992, ApJ, 397, 174
Polygiannakis, J. M., & Moussas, X. 1999, Plasma Phys. Control. Fusion, 41, 967
Pongracic, H., Chapman, S. J., Davies, J. R., et al. 1992, MNRAS, 256, 291
Ricotti, M., Ferrara, A., & Miniati, F. 1997, ApJ, 485, 254
Rohlfs, R., Herbstmeier, U., Mebold, U., & Winnberg, A. 1989, A&A, 211, 402
Serabyn, E., Güsten, R., & Schulz, A. 1993, ApJ, 413, 571
Spitzer, L. 1978, Physical Processes in the Interstellar Medium (New York: Wiley)
Stone, M. E. 1970a, ApJ, 159, 293
Stone, M. E. 1970b, ApJ, 159, 277
Strom, S. E., Strom, K. M., & Edwards, S. 1988, in Galactic and Extragalactic Star Formation, ed. R. E. Pudritz, & M. Fich (Dordrecht: Kluwer), 53
Vallée, J. P. 1995, AJ, 110, 2256
Vrba, F. J., Coyne, G. V., & Tapia, S. 1981, ApJ, 243, 489
Vrba, F. J., Strom, S. E., & Strom, K. M. 1976, AJ, 81, 958
Vrba, F. J., Strom, S. E., & Strom, K. M. 1988, AJ, 96, 680
Whitworth, A. P. 1998, MNRAS, 296, 442
Zeldovich, Ya. B., Ruzmaikin, A. A., & Sokoloff, D. D. 1983, Magnetics Fields in Astrophysics (New York: Gordon & Breach)
Zweibel, E. G. 1999, Physics of Plasma, 6, 1725